

KILOPARSEC-SCALE JETS IN THREE RADIO-LOUD NARROW-LINE SEYFERT 1 GALAXIES

JOSEPH L. RICHARDS^{*} AND MATTHEW L. LISTER

Department of Physics and Astronomy, Purdue University, 525 Northwestern Ave, West Lafayette, IN 47907, USA

Draft version January 23, 2015

ABSTRACT

We have discovered kiloparsec-scale extended radio emission in three narrow-line Seyfert 1 galaxies (NLS1s) in sub-arcsecond resolution 9 GHz images from the Karl G. Jansky Very Large Array (VLA). We find all sources show two-sided, mildly core-dominated jet structures with diffuse lobes dominated by termination hotspots. These span 20–70 kpc with morphologies reminiscent of FR II radio galaxies, while the extended radio luminosities are intermediate between FR I and FR II sources. In two cases the structure is linear, while a 45° bend is apparent in the third. Very Long Baseline Array images at 7.6 GHz reveal parsec-scale jet structures, in two cases with extended structure aligned with the inner regions of the kiloparsec-scale jets. Based on this alignment, the ratio of the radio core luminosity to the optical luminosity, the jet/counter-jet intensity and extension length ratios, and moderate core brightness temperatures ($\lesssim 10^{10}$ K), we conclude these jets are mildly relativistic ($\beta \lesssim 0.3$, $\delta \sim 1 - 1.5$) and aligned at moderately small angles to the line of sight (10–15°). The derived kinematic ages of $\sim 10^6$ – 10^7 y are much younger than radio galaxies but comparable to other NLS1s. Our results increase the number of radio-loud NLS1s with known kiloparsec-scale extensions from seven to ten and suggest that such extended emission may be common, at least among the brightest of these sources.

Subject headings: galaxies: active — galaxies: jets — galaxies: Seyfert — galaxies: individual (J0953+2836, J1435+3131, J1722+5654) — radio continuum: galaxies

1. INTRODUCTION

Narrow-line Seyfert 1 galaxies (NLS1s) are a peculiar class of active galactic nuclei (AGN). They resemble ordinary Seyfert 1 galaxies but their optical broad lines are narrower ($\text{FWHM}(H\beta) \leq 2000 \text{ km s}^{-1}$). The black hole masses of NLS1s are relatively small (10^5 – $10^8 M_\odot$; e.g., Zhou et al. 2006) and their accretion rates are high, often a substantial fraction of the Eddington rate (Boller et al. 1996). It has, however, been suggested that this is a result of systematic underestimation of the black hole masses (Decarli et al. 2008; Marconi et al. 2008; Calderone et al. 2013). About 7% of known NLS1s are radio-loud (Komossa et al. 2006) and it is clear that jets are present in some of these (e.g., Zhou et al. 2003; Yuan et al. 2008). The detection of gamma-ray emission from several radio-loud NLS1s provides evidence that these jets are relativistic (e.g., Abdo et al. 2009). This was unexpected because jets in AGN are typically associated with large black holes, while high accretion rates in stellar-mass black hole binaries normally correspond to quenched-jet states (e.g., Boroson 2002; Maccarone et al. 2003). Study of the jets in NLS1s will therefore help us understand how the processes underlying jet production scale with black hole mass (e.g., Heinz & Sunyaev 2003; Foschini 2012).

Radio emission on kiloparsec scales has been found in only a few NLS1s. Together, Whalen et al. (2006), Antón et al. (2008), Gliozzi et al. (2010), and Doi et al. (2012) reported six examples from the 1.4 GHz Faint Images of the Radio Sky at Twenty centimeters (FIRST) survey (Becker et al. 1995) and 4.8 GHz Australian Telescope Compact Array (ATCA) observations. The resolution of these observations was limited, however. The 5'' FIRST beam only resolves sources $\gtrsim 2''$, while the ATCA beam was about a factor of two better. NLS1s

are known out to $z = 0.8$ so this corresponds to $\gtrsim 10$ kpc, leaving a range of kiloparsec scales largely unexplored. Recently, Doi et al. (2014) reported extended emission in a radio-quiet NLS1.

In this work, we present the detection of kiloparsec-scale radio emission in three radio-loud NLS1s (J0953+2836, J1435+3131, and J1722+5654). These are the first such detections in these sources, all of which were detected but unresolved by the FIRST survey (White et al. 1997). This increases the number of radio-loud NLS1s known to be extended on kiloparsec scales from seven to ten. We also present parsec-scale radio images showing bright jet-like structures. Where necessary, we have assumed a flat Λ -Cold Dark Matter cosmology with $\Omega_\Lambda = 0.7$ and $H_0 = 70 \text{ km s}^{-1} \text{ Mpc}^{-1}$. Spectral indices are specified with flux density $S_\nu \propto \nu^\alpha$ at frequency ν . Velocities are quoted as fractions of the speed of light, $\beta = v/c$.

2. OBSERVATIONS AND DATA REDUCTION

We observed three radio-loud NLS1s with the Karl G. Jansky Very Large Array (VLA) and the Very Long Baseline Array (VLBA). The VLA observations were made to obtain radio coordinates accurate enough for correlation as part of a VLBA program monitoring the 15 known radio-loud NLS1s above 0° declination with archival centimeter-band flux densities exceeding 30 mJy. (Richards et al., in prep.). Among the 15, only these three lacked sufficiently precise coordinates. Properties of our targets and our refined coordinates are listed in Table 1.

The VLA observations were made on 15 Feb 2014 and consisted of a single 10 minute snapshot of each source sandwiched between short observations of a nearby phase calibrator with a known position (better than 2 mas). A short scan on 3C 286 was used to calibrate the flux density scale, applying the appropriate model to account for resolved structure. At the

^{*}jl@purdue.edu

time of observation, the VLA was transitioning from BnA to A configuration, with 27 active antennas on baselines ranging from 0.3 to 31.5 km. The X-band receiver provided 2 GHz bandwidth centered on 9 GHz, which was sampled with the 8-bit sampler with 2 s integration time. Requantizer gains were applied and the data were converted to UVFITS format using CASA (McMullin et al. 2007). The data were then calibrated in AIPS following the standard procedures in the AIPS Cookbook and deconvolved, self-calibrated, and imaged in DIFMAP (Shepherd et al. 1994). After initial calibration of the phase calibrators, cycles of phase-only self-calibration and CLEAN were repeated until a few times the residual root-mean-square (rms) noise level was reached. Amplitude self-calibration was then applied to determine the final complex gains. To measure source positions, the gains derived from the phase calibrators were interpolated onto the science observations. A circular Gaussian component model of the core region was fitted to the visibilities and the position of the brightest component is reported in Table 1, accurate to about 0.1 beam, or about 15 mas. For imaging, the science target data were cleaned and self-calibrated using the same procedures used for the phase calibrators.

VLBA observations were made on 8 Feb 2014 using the wideband C-band receiver configured to provide 256 MHz total bandwidth in 8 sub-bands equally spaced over the 480 MHz band centered on 7.632 GHz with good weather at all 10 antennas. The total integration time, listed in Table 1, was split into scans separated in time to provide good (u, v) coverage. In each scan, 49 s of full polarization data were recorded as 2-bit samples for a total 2 Gbps data rate, with science target observations interleaved with observations of a nearby phase reference. Observations at 4.9, 15.4, and 23.8 GHz were also carried out, but we report only 7.632 GHz total intensity results here. Full results from the VLBA program, including polarization measurements and the other frequencies, will be reported elsewhere. After correlation with the DiFX correlator (Deller et al. 2007) using our refined coordinates, the phase-referenced VLBA data were processed following the AIPS Cookbook, applying gain solutions from the phase references to the science targets. A CLEAN model was constructed, then phase-only self-calibration with a 10 minute solution interval was applied and a final CLEAN was performed. We verified our flux density scale, accurate to about 5%, by comparing several calibrators with preliminary results from Effelsberg 100 m telescope observations made by the *Fermi*-GST AGN Multi-frequency Monitoring Alliance (F-GAMMA; Fuhrmann et al. 2007; Angelakis et al. 2010).

3. RESULTS

The maps we obtained from our observations are shown in Figures 1, 2, and 3 and Table 2 lists quantities computed from our results. Using 1.4 GHz FIRST flux densities and our 9 GHz VLA flux densities, we have determined the non-simultaneous spectral index α . The formal uncertainty is ± 0.04 , assuming 5% uncertainties for the flux densities, not accounting for non-simultaneity. These spectral indices are lower limits because our higher resolution maps may resolve out more extended emission than in the FIRST data.

On kiloparsec scales, all of these sources show similar morphologies. The emission is dominated by a bright core straddled by a pair of extended lobes. These lobes are edge-brightened, terminating in hotspots. Like in FR II radio galaxies, the ratios of the hotspot separations to the full extents of the sources exceed 0.5 (Fanaroff & Riley 1974). Extended

emission between the bright core and the brighter of the two lobes is found in all sources, while the fainter lobe is relatively isolated. On parsec scales, we find an isolated core in J1435+3131 while the others show extension roughly aligned with the kiloparsec-scale structure.

3.1. J0953+2836

The emission in the tapered VLA map of J0953+2836 (Figure 1) spans $10.^{\prime\prime}1$ (measured at the second contour, following Scheuer (1995)), a projected length of 70.2 kpc. The brighter lobe lies along position angle (PA) 212° , measured north through east. From the VLBA map, the parsec-scale image shows extended emission with a ridge along PA 232° . The ridge brightens slightly toward the SW. A two-component Gaussian model fits the visibilities well, with the SW component brighter by a factor of 1.2. Identification of the parsec-scale core is uncertain and it is unclear whether this is a one- or two-sided jet.

3.2. J1435+3131

The kiloparsec-scale emission in J1435+3131 (Figure 2) spans $5.^{\prime\prime}00$, or a projected length of 30.6 kpc. A sharp bend is evident between the core and the NE kiloparsec-scale lobe. A narrow, continuous trail of emission exits northward from the core, then bends about 45° to the northeast, terminating in a faint knot. A straight line extended from this knot along the direction after the bend is closely aligned with the brighter of two hotspots in the disconnected radio lobe. The parsec-scale image shows only a compact core. No kiloparsec-scale emission is evident between the core and the fainter SW radio lobe, which has a single hotspot.

3.3. J1722+5654

On kiloparsec scales, J1722+5654 (Figure 3) contains a bright central core straddled by a linear structure along PA 47° . The emission spans $4.^{\prime\prime}08$ which corresponds to a 22.8 kpc projected length. The parsec-scale structure is also linear, with three apparent emission regions along PA 60° . The brightest parsec-scale emission is from the SW component; if this is identified as the core, then the parsec-scale morphology is a one-sided jet directed toward the brighter kiloparsec-scale lobe. This component is 2.3 times brighter than the NE component. We note that the structure could also be interpreted as a two-sided jet with a faint core at the central emission region, in which case the brighter ejected component is directed toward the fainter kiloparsec-scale lobe. Misalignments as large as 180° between the parsec- and kiloparsec-scale jets have been seen (Kharb et al. 2010). However, the brightness temperature of the SW component is more than 20 times higher than either other component, which favors its identification as the core (see Section 4.3).

4. DISCUSSION

4.1. Morphologies

The parsec- and kiloparsec-scale morphologies of these three sources are similar to those found in other jetted AGN. Their kiloparsec scale morphologies resemble those found in blazars, radio galaxies, and other radio-loud NLS1s (Cooper et al. 2007; Kharb et al. 2010; Doi et al. 2012). Extended two-sided emission is present in all three cases, with one lobe substantially brighter than the other, presumably because it is approaching us. These resemble FR II radio galaxies, with

TABLE 1
SOURCE PROPERTIES AND REFINED J2000 COORDINATES.

Source	NVSS Name	z	M_{BH} ($10^7 M_{\odot}$)	$S_{1.4}$ (mJy)	M_V	R.A. (h m s)	Decl. ($^{\circ} \text{ } '$)	Phase Reference VLA / VLBA (9)	VLBA Time (min)
(1)	(2)	(3)	(4)	(5)	(6)	(7)	(8)	(9)	(10)
J0953+2836	J095317+283601	0.659	6.3	47.94	-24.04	09 53 17.102	28 36 01.559	J0956+2515 / J0954+2639	4.8
J1435+3131	J143509+313149	0.502	3.2	44.72	-23.01	14 35 09.495	31 31 47.864	J1435+3012 / J1422+3223	9.8
J1722+5654	J172206+565452	0.426	2.5	39.83	-23.58	17 22 06.029	56 54 51.696	J1657+5705 / J1727+5510	13.0

NOTE. — Columns are as follows: (1) IAU name (J2000); (2) corresponding source in the NRAO VLA Sky Survey (NVSS, Condon et al. 1998); (3) redshift from Hewett & Wild (2010); (4) black hole mass from Yuan et al. (2008); (5) integrated 1.4 GHz flux density from White et al. (1997); (6) absolute V-band magnitude computed from Sloan Digital Sky Survey Data Release 10 (Ahn et al. 2014) g and r magnitudes using $V = g - 0.52(g-r) - 0.03$, after Jester et al. (2005) with no correction for galactic extinction; (7)-(8) new J2000 coordinates determined from our VLA observations with an uncertainty of ± 15 mas; (9) IAU name (J2000) of phase calibrators used for VLA and VLBA observations; (10) total VLBA integration time.

TABLE 2
MEASURED PROPERTIES.

Source	ℓ_{proj} (kpc)	$S_{\text{core},9}^{\text{kpc}}$ (mJy)	$S_{\text{tot},9}^{\text{kpc}}$ (mJy)	$\mathcal{I}_9^{\text{hsj}}$ ($\mu\text{Jy beam}^{-1}$)	α	$L_{1.4}^{\text{ext}}$ (W Hz $^{-1}$)	R_{hs}	$\log R_V$	$(\beta \cos \theta)_{\text{hs}}$	$(\beta \cos \theta)_x$	Age (10^6 y)	$S_{\text{core},7.6}^{\text{pc}}$ (mJy)	$S_{\text{tot},7.6}^{\text{pc}}$ (mJy)	T_B (10^8 K)
(1)	(2)	(3)	(4)	(5)	(6)	(7)	(8)	(9)	(10)	(11)	(12)	(13)	(14)	(15)
J0953+2836	70.2	12.0	18.8	158	-0.50	25.9	1.9	1.94	0.082	0.028	14–22	4.35	10.0	1.2
J1435+3131	30.6	7.8	11.7	324	-0.72	25.4	2.2	1.90	0.098	0.15	1.3–2.0	5.1	5.5	4.8
J1722+5654	22.8	7.9	12.2	688	-0.64	25.3	13	1.52	0.31	0.20	0.6–1.0	5.4	10.2	9.8

NOTE. — Columns are as follows: (1) IAU name (J2000); (2) projected full span of extended radio emission; (3)-(4) flux density of the core component and the total integrated flux density from the 9 GHz VLA data; (5) peak intensity of the 9 GHz emission in the approaching lobe; (6) non-simultaneous 1.4–9 GHz spectral index; (7) extended isotropic luminosity, extrapolated from 9 GHz to 1.4 GHz and k -corrected assuming $\alpha_{\text{ext}} = -1$; (8) ratio of peak intensity of approaching and receding lobes; (9) ratio of optical to radio core luminosity, k -corrected to the emission frame assuming $\alpha_{\text{core}} = 0$, $\alpha_{\text{ext}} = -1$, and $\alpha_{\text{optical}} = -0.5$; (10) projected jet speed computed from R_{hs} ; (11) projected jet speed computed from jet/counter-jet length ratio; (12) kinematic age of source implied by $(\beta \cos \theta)_x$ for $\theta = 10\text{--}15^{\circ}$; (13) 7.6 GHz VLBA core flux density; (14) total 7.6 GHz VLBA flux density; (15) emission frame VLBA core brightness temperature.

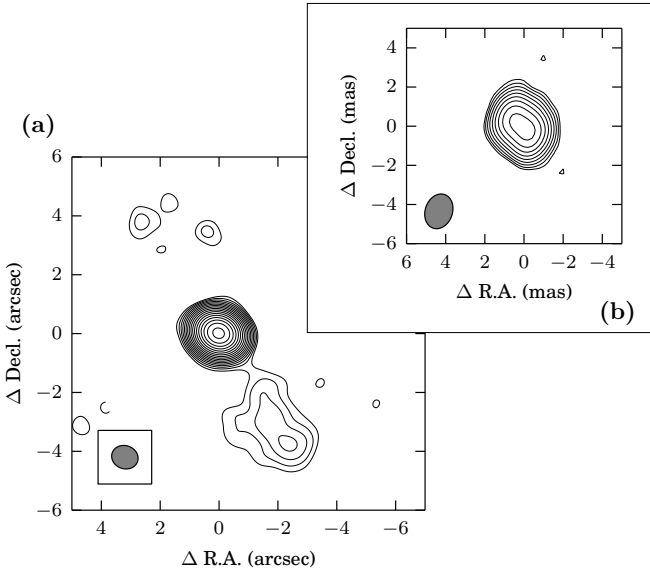


FIG. 1.— Naturally weighted maps of J0953+2836. Contours increase by factors of $\sqrt{2}$. At this redshift, $1'' = 6.97$ kpc. (a) VLA map (9 GHz). To emphasize low-surface brightness extended features, a Gaussian taper with half-maximum at 1.5×10^5 wavelengths has been applied. The first contour is at $50 \mu\text{Jy beam}^{-1}$, about three times the map rms of $17 \mu\text{Jy beam}^{-1}$, and the map peaks at $14.6 \text{ mJy beam}^{-1}$. The elliptical Gaussian restoring beam is shown (FWHM $0.911'' \times 0.786''$). (b) VLBA map (7.6 GHz) of the central bright feature. The first contour is at $0.3 \text{ mJy beam}^{-1}$, about three times the map rms of $0.1 \text{ mJy beam}^{-1}$, and the map peaks at $5.7 \text{ mJy beam}^{-1}$. The elliptical Gaussian restoring beam is shown (FWHM $1.82 \text{ mas} \times 1.39 \text{ mas}$)

brightened hotspots near the outer edges of the kiloparsec-scale lobes evident at least on the approaching side. All three sources are moderately core dominated at these scales, with about 2/3 of the total emission in the kiloparsec core. The

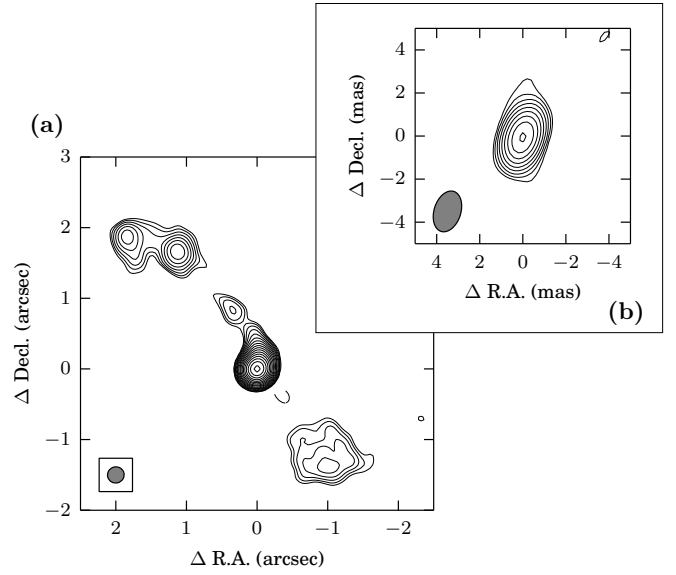


FIG. 2.— Naturally weighted maps of J1435+3131. Contours increase by factors of $\sqrt{2}$. At this redshift, $1'' = 6.12$ kpc. (a) VLA map (9 GHz). The first contour is at $30 \mu\text{Jy beam}^{-1}$, about five times the map rms noise of $6 \mu\text{Jy beam}^{-1}$, and the map peaks at $8.39 \text{ mJy beam}^{-1}$. The elliptical Gaussian restoring beam is shown (FWHM $0.236'' \times 0.228''$). (b) VLBA map (7.6 GHz) of the central bright feature. The first contour is at $0.3 \text{ mJy beam}^{-1}$, about three times the map rms noise of $0.1 \text{ mJy beam}^{-1}$, and the map peaks at $5.0 \text{ mJy beam}^{-1}$. The elliptical Gaussian restoring beam is shown (FWHM $1.95 \text{ mas} \times 1.24 \text{ mas}$)

extended isotropic luminosities $L_{1.4}^{\text{ext}}$, computed by subtracting the fitted core flux density from the total flux density and scaling to 1.4 GHz assuming a spectral index $\alpha_{\text{ext}} = -1$, lie in the transition range between FR I and FR II galaxies, and fall

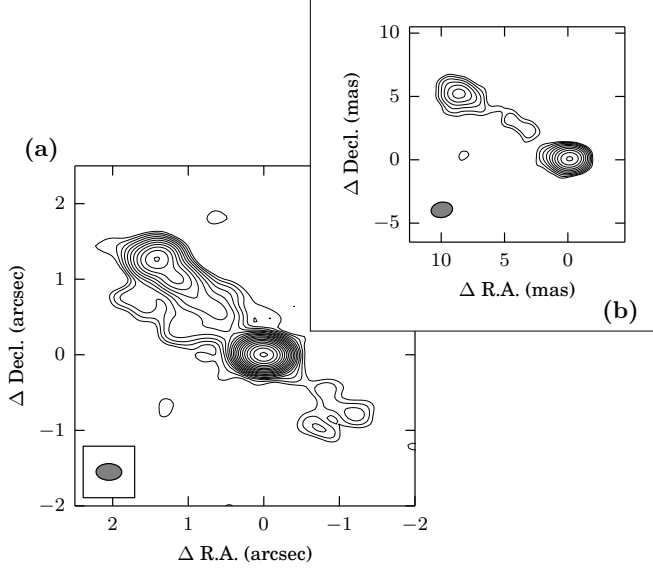


FIG. 3.— Naturally weighted maps of J1722+5654. Contours increase by factors of $\sqrt{2}$. At this redshift, $1'' = 5.58$ kpc. (a) VLA map (9 GHz). The first contour is at $21 \mu\text{Jy beam}^{-1}$, about three times the map rms noise of $7 \mu\text{Jy beam}^{-1}$, and the map peaks at $8.14 \text{ mJy beam}^{-1}$. The elliptical Gaussian restoring beam is shown (FWHM $0.341'' \times 0.221''$). (b) VLBA map (7.6 GHz) of the central bright feature. The first contour is at $0.2 \text{ mJy beam}^{-1}$, about three times the map rms noise of $0.07 \text{ mJy beam}^{-1}$, and the map peaks at $4.8 \text{ mJy beam}^{-1}$. The elliptical Gaussian restoring beam is shown (FWHM $1.71 \text{ mas} \times 1.21 \text{ mas}$).

along the $L - z$ trend reported in Kharb et al. (2010).

On parsec scales, the sources are compatible with one-sided jet morphologies. The parsec-scale core region in J1435+3131 is especially blazar-like, consisting only of a compact core. The other two sources are compatible with an alternative interpretation as a faint or undetected core with two-sided emission.

4.2. Viewing Angles

Two lines of reasoning suggest that the jet axes in these sources are at relatively small angles to the line of sight. First, the extended parsec-scale jets, where detected, are aligned with the kiloparsec-scale jets (this would not be true for J1722+5654 if it is misaligned by about 180°). Misalignments due to projection effects are expected to be more common for small viewing angles, so the alignment we find suggests the viewing angles are not especially small, although our statistics are limited (Pearson & Readhead 1988).

Second, we reach a similar conclusion from R_V , the ratio of the observed radio core luminosity to the optical luminosity. The latter acts as a proxy for the unbeamed, intrinsic emission. Motivated by Wills & Brotherton (1995), Kharb et al. (2010) found R_V to be a good indicator of viewing angle, where $\log R_V = \log L_{\text{core}} - \log M_{\text{abs}} - 13.69$ with L_{core} the 1.4 GHz core luminosity and M_{abs} the k -corrected optical V-band magnitude. Assuming a flat core spectral index, we find that the $\log R_V$ values for these NLS1s (1.5–1.9) are at the low end of the distribution for jet-selected radio-loud AGN (e.g., the MOJAVE sample; Lister et al. 2013; Kharb et al. 2010). This suggests the viewing angles of these NLS1s are similar to the highest angles in the MOJAVE sources, roughly $10\text{--}15^\circ$ (Savolainen et al. 2010).

4.3. Jet Speeds

Assuming the structure and evolution of these sources is intrinsically symmetric, we can estimate the projected jet speed in two ways. This common assumption is supported in these particular cases by the alignment of the approaching parsec-scale jet and the longer kiloparsec-scale lobe (Arshakian & Longair 2000). Both methods have a degeneracy between the speed and the viewing angle θ , but assuming $\theta \gtrsim 10^\circ$, as seems to be the case, $\beta \cos \theta \sim \beta$ to within the likely accuracy of our measurements. First, we consider the flux ratio between the hotspots in the approaching and receding jets. If absorption is negligible along the additional optical path to the counter-jet, the expected ratio is

$$R_{\text{hs}} = \left(\frac{1 + (\beta \cos \theta)_{\text{hs}}}{1 - (\beta \cos \theta)_{\text{hs}}} \right)^{3-\alpha}, \quad (1)$$

where $(\beta \cos \theta)_{\text{hs}}$ is the projected speed at which the lobes advance at angle θ to the line of sight. For this calculation, we use the ratio of the peak intensity (in $\mu\text{Jy beam}^{-1}$) between the jet and counter-jet lobes, $(R_{\text{hs}} = \mathcal{I}_9^{\text{hs,j}} / \mathcal{I}_9^{\text{hs,cj}})$. We obtain similar results if we instead use the ratio between the flux densities obtained by fitting a Gaussian component model. For J0953+2836 and J1722+5654, if we interpret the parsec-scale jets as two-sided, the flux density ratios of 1.2 and 2.3 imply jet speeds $\beta \cos \theta = 0.04$ and 0.18, comparable to those found at kiloparsec scales.

We can also examine the asymmetry in length between the jet and counter-jet. If the structure is intrinsically symmetric, differential light travel time will cause the approaching jet to appear longer than the receding jet (Banhatti 1980). In this case, the ratio $x \equiv (r_j - r_{\text{cj}}) / (r_j + r_{\text{cj}}) = (\beta \cos \theta)_x$ where r_j and r_{cj} are the lengths of the jet and counter-jet, and $(\beta \cos \theta)_x$ is the jet speed estimate. This method gives comparable results to the beaming ratio method, so overall we find $\beta \cos \theta \sim 0.03\text{--}0.3$. These correspond to Doppler factors in the range $\delta = 1\text{--}1.5$, where $\delta = (1 - \beta^2)^{1/2} / (1 - \beta \cos \theta)$.

Doppler beaming will increase the apparent brightness temperature of an emitting region relative to its intrinsic brightness temperature, $T_{\text{B,int}}$, with the observed $T_{\text{B}} = \delta T_{\text{B,int}}$. Using our VLBA data, we computed T_{B} in the emission frame from an elliptical Gaussian model as $T_{\text{B}} = (1.22 \times 10^{12} \text{ K}) \times S(1 + z) / (a_{\text{maj}} a_{\text{min}} v^2)$ where v is the observing frequency in GHz and S , a_{maj} , and a_{min} are the flux density in janskys and the major and minor axis FWHMs (in mas) of the core component. The brightness temperatures we find are all substantially below the equipartition limit of about 10^{11} K , compatible with a low Doppler factor (Readhead 1994). In each source, the presumed core has the highest brightness temperature of all fitted components by at least a factor of eight.

The kinematic ages of these sources, computed assuming the approaching hotspots advanced outward steadily at their current speeds ($\beta \sim 0.03\text{--}0.3$) at a viewing angle $\theta \sim 10\text{--}15^\circ$, are found to be a few times $10^5\text{--}10^7 \text{ y}$. These are in the range found for other extended radio-loud NLS1s, consistent with NLS1s being much younger than blazars or radio galaxies (Doi et al. 2012).

5. CONCLUSIONS

Extended emission on kiloparsec scales was detected in all three of our targets. This is perhaps surprising in light of the small number of spatially extended NLS1s previously known. However, few have been observed with the requisite angular resolution and sensitivity to detect the extensions we found

here. Because our targets were arbitrarily selected from a parent sample of bright, radio-loud NLS1s, there was no reason all three were especially likely to show extended emission. Thus, our findings suggest that other NLS1s in the parent sample are also likely to be extended. Observations of a larger sample are needed to verify this and, if true, to investigate whether this is generally true of all radio-loud NLS1s or is a peculiar property of the parent sample. The morphologies of these sources on both kiloparsec and parsec scales are consistent with the presence of a mildly relativistic jet at a moderately small ($10\text{--}15^\circ$) angle to the line of sight. The three sources we observed and most previously known extended NLS1s where resolution permitted classification show FR II-like edge-brightened lobes. In contrast, Doi et al. (2014) recently reported edge-darkened FR I-like extended radio emission in the NLS1 Mrk 1239. The latter is radio quiet, while the others are radio loud, suggesting that radio loudness may be connected to intrinsic source properties, such as jet power, rather than orientation effects.

The authors thank T. G. Arshakian for helpful suggestions and E. Angelakis and the F-GAMMA program for sharing the preliminary data we used to check our VLBA calibration. This work was supported by the National Aeronautics and Space Administration (NASA) through *Fermi* Guest Investigator grant NNX13AO79G. The National Radio Astronomy Observatory is a facility of the National Science Foundation operated under cooperative agreement by Associated Universities, Inc. This work made use of the Swinburne University of Technology software correlator, developed as part of the Australian Major National Research Facilities Programme and operated under licence. This research has made use of the NASA/IPAC Extragalactic Database (NED) which is operated by the Jet Propulsion Laboratory, California Institute of Technology, under contract with the National Aeronautics and Space Administration. This work made use of Ned Wright's Javascript Cosmology Calculator (Wright 2006).

REFERENCES

Abdo, A. A., et al. 2009, *ApJ*, 707, L142
 Ahn, C. P., et al. 2014, *ApJS*, 211, 17
 Angelakis, E., Fuhrmann, L., Nestoras, I., Zensus, J. A., Marchili, N., Pavlidou, V., & Krichbaum, T. P. 2010, in Proceedings of the Workshop “Fermi meets Jansky - AGN in Radio and Gamma-Rays”, ed. T. Savolainen, E. Ros, R. W. Porcas, & J. A. Zensus, arXiv:1006.5610
 Antón, S., Browne, I. W. A., & Marchá, M. J. 2008, *A&A*, 490, 583
 Arshakian, T. G., & Longair, M. S. 2000, *MNRAS*, 311, 846
 Banhatti, D. G. 1980, *A&A*, 84, 112
 Becker, R. H., White, R. L., & Helfand, D. J. 1995, *ApJ*, 450, 559
 Boller, T., Brandt, W. N., & Fink, H. 1996, *A&A*, 305, 53
 Boroson, T. A. 2002, *ApJ*, 565, 78
 Calderone, G., Ghisellini, G., Colpi, M., & Dotti, M. 2013, *MNRAS*, 431, 210
 Condon, J. J., Cotton, W. D., Greisen, E. W., Yin, Q. F., Perley, R. A., Taylor, G. B., & Broderick, J. J. 1998, *AJ*, 115, 1693
 Cooper, N. J., Lister, M. L., & Kochaneczyk, M. D. 2007, *ApJS*, 171, 376
 Decarli, R., Dotti, M., Fontana, M., & Haardt, F. 2008, *MNRAS*, 386, L15
 Deller, A. T., Tingay, S. J., Bailes, M., & West, C. 2007, *PASP*, 119, 318
 Doi, A., Nagira, H., Kawakatu, N., Kino, M., Nagai, H., & Asada, K. 2012, *ApJ*, 760, 41
 Doi, A., Wajima, K., Hagiwara, Y., & Inoue, M. 2014, ArXiv e-prints, arXiv:1412.3308
 Fanaroff, B. L., & Riley, J. M. 1974, *MNRAS*, 167, 31P
 Foschini, L. 2012, in American Institute of Physics Conference Series, Vol. 1505, American Institute of Physics Conference Series, ed. F. A. Aharonian, W. Hofmann, & F. M. Rieger, 574–577
 Fuhrmann, L., Zensus, J. A., Krichbaum, T. P., Angelakis, E., & Readhead, A. C. S. 2007, in American Institute of Physics Conference Series, Vol. 921, The First GLAST Symposium, ed. S. Ritz, P. Michelson, & C. A. Meegan, 249–251
 Gliozzi, M., Papadakis, I. E., Grupe, D., Brinkmann, W. P., Raeth, C., & Kedziora-Chudczer, L. 2010, *ApJ*, 717, 1243
 Heinz, S., & Sunyaev, R. A. 2003, *MNRAS*, 343, L59
 Hewett, P. C., & Wild, V. 2010, *MNRAS*, 405, 2302
 Jester, S., et al. 2005, *AJ*, 130, 873
 Kharb, P., Lister, M. L., & Cooper, N. J. 2010, *ApJ*, 710, 764
 Komossa, S., Voges, W., Xu, D., Mathur, S., Adorf, H.-M., Lemson, G., Duschl, W. J., & Grupe, D. 2006, *AJ*, 132, 531
 Lister, M. L., et al. 2013, *AJ*, 146, 120
 Maccarone, T. J., Gallo, E., & Fender, R. 2003, *MNRAS*, 345, L19
 Marconi, A., Axon, D. J., Maiolino, R., Nagao, T., Pastorini, G., Pietrini, P., Robinson, A., & Torricelli, G. 2008, *ApJ*, 678, 693
 McMullin, J. P., Waters, B., Schiebel, D., Young, W., & Golap, K. 2007, in Astronomical Society of the Pacific Conference Series, Vol. 376, Astronomical Data Analysis Software and Systems XVI, ed. R. A. Shaw, F. Hill, & D. J. Bell, 127
 Pearson, T. J., & Readhead, A. C. S. 1988, *ApJ*, 328, 114
 Readhead, A. C. S. 1994, *ApJ*, 426, 51
 Savolainen, T., Homan, D. C., Hovatta, T., Kadler, M., Kovalev, Y. Y., Lister, M. L., Ros, E., & Zensus, J. A. 2010, *A&A*, 512, A24
 Scheuer, P. A. G. 1995, *MNRAS*, 277, 331
 Shepherd, M. C., Pearson, T. J., & Taylor, G. B. 1994, in Bulletin of the American Astronomical Society, Vol. 26, Bulletin of the American Astronomical Society, 987–989
 Whalen, D. J., Laurent-Muehleisen, S. A., Moran, E. C., & Becker, R. H. 2006, *AJ*, 131, 1948
 White, R. L., Becker, R. H., Helfand, D. J., & Gregg, M. D. 1997, *ApJ*, 475, 479
 Wills, B. J., & Brotherton, M. S. 1995, *ApJ*, 448, L81
 Wright, E. L. 2006, *PASP*, 118, 1711
 Yuan, W., Zhou, H. Y., Komossa, S., Dong, X. B., Wang, T. G., Lu, H. L., & Bai, J. M. 2008, *ApJ*, 685, 801
 Zhou, H., Wang, T., Yuan, W., Lu, H., Dong, X., Wang, J., & Lu, Y. 2006, *ApJS*, 166, 128
 Zhou, H.-Y., Wang, T.-G., Dong, X.-B., Zhou, Y.-Y., & Li, C. 2003, *ApJ*, 584, 147